Supporting Information

Promoting the four electrocatalytic reactions of OER/ORR/HER/MOR by using multi-component metal sulfide heterostructure for the zinc-air batteries and water splitting

Jiaxin Dang [a], Genman Chen [a], Bingen Yuan [a], Fuyue Liu [a], Qin Wang [b], Fu Wang [a], He Miao [a, *], Jinliang Yuan [a]

[a] Faculty of Maritime and Transportation, Ningbo University, Ningbo 315211, PR China

[b] Department of Microelectronic Science and Engineering, Faculty of Science, Ningbo University, Ningbo 315211, PR China

* Corresponding authors:

Prof. He Miao, E-mail: miaohe@nbu.edu.cn

1. Reagents and chemicals

Cobalt nitrate ($Co(NO_3)_2 \cdot 6H_2O$), Sodium sulphate (Na_2SO_4), Aminothiourea (CH_5N_3S), Nafion (5 wt.%), polytetrafluoroethylene (PTFE), anhydrous ethanol (C_2H_5OH), carbon (XC-72), acrylamide (AM), ammonium persulfate (APS), N, N'-Methylenebis (acrylamide) (MBA), acrylic acid (AA), dimethyl sulfoxide (DMSO), glycerol ($C_3H_8O_3$), cellulose nanofibers, polyvinyl alcohol (PVA), potassium hydroxide (KOH), anhydrous methanol (CH_3OH), zinc acetate ($Zn(Ac)_2$), and zinc foil (thickness of 0.15 mm) were supplied by Aladdin Industrial Co., Ltd. (Shanghai, China). Among them, all chemical reagents were analytical grade. Iron-nickel foam (INF, Ni: Fe = 3: 7, thickness of 1.5 mm) was obtained from Suzhou Keshenghe Metal Materials Co., Ltd. Cobalt foil (thickness of 0.1 mm) was purchased from Qinghe County Lisheng Metal Materials Co., Ltd. (Purity of 99.9%). All chemicals were used as received without further purification. The water used in all experiments was ultrapure (18.2 MΩ·cm). Seawater was taken from the East China Sea, 29°52000.00" N, 121°31000.00" E.

2. Material characterizations

X-ray diffraction (XRD) patterns were obtained on a Bruker D8 Advance X-ray diffract meter (Cu Kα = 1.5418 Å) at a scanning rate of 0.02° s^{-1} from 20° to 90°. The microstructure and elemental distribution of the synthesized samples were observed using field emission scanning electron microscopy (FESEM, Hitachi S4800, 5 kV), transmission electron microscopy (TEM, JF-20, Hitachi), and high-resolution transmission electron microscopy (HRTEM, JF-20, Hitachi). X-ray photoelectron

spectroscopy (XPS) was performed on an AXISULTARDLD spectroscopy spectrometer with an Al-Kα X-ray source.

3. Electrochemical measurements

The working electrode was subjected to electrochemical LSV testing using a standard three-electrode system on the electrochemical workstation CHI 760 E (Shanghai Chenhua Instrument Co., Ltd.) at room temperature of 25 ± 0.2 °C. The working electrode was either a self-supported sample (1 x 1 cm^2) prepared in the experiment or a catalyst-coated rotating disc electrode (RDE) (0.196 cm^2). The reference electrode was Hg/HgO, and the counter electrode was a graphite rod. The graphite rod and Hg/HgO electrodes were provided by Shanghai Ledun Industrial Co., Ltd and CHI Instruments, Inc, respectively. 0.1/1.0 M KOH solution was used as electrolyte. The catalyst slurry for preparing the working electrode with RDE was a mixed solution containing 5 mg sample powder (scraped from INF), 5 mg carbon (Vulcan XC-72), 80 μL 5 wt.% Nafion and 2 mL ethanol. After sufficiently ultrasonic mixing, 20 μL of the dispersion was extracted and uniformly dropped on the glassy carbon (GC) electrode.

For the preparation of the Pt/C ink, 5 mg Pt/C (20 wt.%) and 80 μL Nafion (5 wt.%) were dispersed in 2 mL ethanol solution through ultrasonic treatment. For the preparation of the RuO$_2$ ink, 5 mg RuO$_2$, 5 mg carbon (Vulcan-XC72) and 80 μL Nafion (5 wt.%) were dispersed in 2 mL ethanol solution through ultrasonic treatment. The inks were evenly dropped on INF (1 × 1 cm^2) to prepare the working electrodes with catalyst loading of 2 mg cm^{-2},

and marked as 20% Pt/C-INF and RuO_2-INF, respectively.

The OER LSV tests were performed in an O_2-saturated 1.0 M KOH solution with a potential range of 0.2 to 1.0 V (vs. Hg/HgO) and a scan rate of 5 mV s^{-1}. The electrodes were activated by the CV scanning before measuring the OER performances. Similarly, the ORR LSV tests were carried out in O_2-saturated 0.1 M KOH solution with a potential range of -0.8 to 0.2 V (vs. Hg/HgO). The HER LSV tests were carried out in N_2-saturated 1.0 M KOH solution with a potential range of -1.6 to -0.8 V (vs. Hg/HgO). The MOR LSV tests were performed in an N_2-saturated in 1.0 M KOH + 1.0 M methanol mixed solution with a potential range of 0.2 to 1.0 V (vs. Hg/HgO) and a scan rate of 5 mV s^{-1}. In the above tests, the LSV curves of OER, ORR, HER and MOR were all tested in the electrolytic cell with the self-supported catalysts, and the ORR LSV curves of the samples were also tested with RDE for comparing with the self-supported catalysts. IR compensation was performed on all the working electrodes, and the following formula was used to convert all recorded potentials into RHE [1]: $E_{RHE} = E_{Hg/HgO} + 0.059 \times pH + 0.098$. Among them, at 25 °C, the overpotential of OER (η) can be determined by the formula: $\eta = E_{RHE} - 1.23$.

The Tafel slopes were obtained from their corresponding linear sweep voltammetry (LSV) by plotting overpotential (η) to the log current (j). The Tafel slopes were calculated from equation $\eta = b* \log j + a$ ('b' is the Tafel slope, and 'a' is a constant) [2].

Chronopotentiometry (CP) tests were adopted to analyze the voltage variation of the working electrode over time within 40000 s to evaluate the OER and HER stability in 1.0 M KOH at a constant current density (100 mA cm^{-2}). Chronoamperometry (CA) tests were used to record the changes in current density of the working electrode over 60000 s to evaluate the ORR durability of the catalysts in 0.1 M KOH solution at the constant voltage (-0.5 V (vs. Hg/HgO)). The CP tests were adopted to analyze the voltage variation of the working electrode over 100000 s to evaluate the MOR durability in 1.0 M KOH + 1.0 M methanol at a constant current (100 mA cm^{-2}).

In order to measure the electrochemical impedance spectroscopy (EIS) of catalysts, the same testing conditions with LSV were configured. The catalysts were used as the working electrode, and an anodic polarization potential of 1.462 V (vs. RHE) was applied to the working electrode. The frequency collection range was set to 10^{-2} - 10^{5} Hz, and the amplitude was set to 5 mV. The tests were conducted on the electrochemical workstation CHI 760 E. Then, the key electrochemical kinetic parameters to evaluate the performance of the catalysts were obtained, that is, the charge transfer resistance (R_{ct}) between the electrode interface and the electrolyte. For EIS testing during MOR, the electrolyte was adopted to a 1.0 M KOH + 1.0 M methanol mixed solution with the applied an anode potential of 1.55 V (vs. RHE), while the other testing conditions remained unchanged. For the

measurement of the electrochemical double-layer capacitance (C_{dl}) of catalysts, CV scans of the samples at different scanning rates (10 to 100 mV s^{-1}) in the potential range of 0.877 to 0.977 V (vs. RHE) were performed in 1.0 M KOH solution. The scanning rate was used as the x-axis, and half of the upper and lower current density corresponding to the intermediate potential values in the scanning interval ($\Delta j = (j_{anode} - j_{cathode})/2$) was used as the y-axis. Then, by fitting the curve, the slope that is the C_{dl} can be obtained. In general, the electrochemically active surface area (ECSA) is proportional to C_{dl} [3, 4]: ECSA $= \dfrac{C_{dl}}{C_s}$ Among them, C_s is the specific capacitance per unit of actual surface area, often replaced by empirical values under assumed conditions.

As mentioned above, the capacitance value of the double layer is related to current density and scanning rate [5]: $C_{dl} = \dfrac{\Delta j}{v}$. Where Δj represents the capacitance current density, v stands for the scanning rate.

For the ECSA tests toward MOR, the electrolyte was uses as 1.0 M KOH+1.0 M methanol mixed solution, and the potential range of 0.867 to 0.967 V (vs. RHE) was set, while the other test conditions kept unchanged.

4. Synthesis of hydrophobic layer

200 g of ethanol was mixed with 6 g of carbon black (Vulcan XC72), and stirred thoroughly at room temperature (25 ± 0.2 ℃) for half an hour. Heat the solution to 35 ℃ and drop polytetrafluoroethylene concentrated dispersion (PTFE, 60 wt.%) into it. After the flocculent precipitate was

formed, press it into the sheets (0.5 mm thickness), and heat it in a annealing furnace at 350 ℃ for 2 h to finally obtain the hydrophobic layer.

5. Synthesis of solid gel electrolyte

The preparation method of alkaline gel electrolyte was as the follows: 8 mg MBA, 10 mg APS, 10 g AM and 8 g cellulose nanofibers were added into a mixed solution of 8 g glycerin and 8 g deionized water at room temperature, and fully stirred to form solution A. Mix 0.64 g of PVA with 5.76 g of deionized water in a high-temperature water bath to form the PVA solvent, and then mix 0.96 g of PVA solvent with 8.64 g of DMSO solution in a high-temperature water bath to form solution B. At room temperature, mix the A and B solution, and then add 1 g AA (acrylic acid) into the mixed solution. After the completely stirring, pour it into a petri dish, and heat it in an oven at 80 ℃ for 1 h to form solid gel (4 mm thickness). Soak it into 6 M KOH + 0.2 M $Zn(Ac)_2$ solution for 20 h at room temperature to obtain the solid gel electrolyte.

6. Assemblies and measurements of ZABs

To estimate the practical applications of the prepared catalysts, they were used as the cathode materials and assembled into aqueous and flexible ZABs. In aqueous ZABs, zinc foil (0.15 mm thickness, 3×3 cm^2), 6 M KOH+0.2 M $Zn(Ac)_2$, and Co-S-INF (or other sample, 1×1 cm^2) electrode were sequentially assembled as the anode, electrolyte, and cathode of the battery, respectively. In the flexible battery, zinc foil (0.15 mm thickness,

2 x 2 cm^2), gel electrolyte and Co-S-INF (1 × 1 cm^2) electrode were assembled as anode, electrolyte and cathode, respectively [6].

All battery tests were conducted at room temperature by using a multi-channel battery testing system (LAND CT2001A, Wuhan Land Electronics Co., Ltd., China). The charge/discharge polarization curves and corresponding power density curves of ZABs at different current densities (mA cm^{-2}) were obtained. To evaluate the cycling stability of ZABs, the tests were conducted at different current densities and cycling times. In aqueous ZAB, the cycle was conducted for 30 min (15 min charge and 15 min discharge) at a current density of 10 mA cm^{-2}. Additionally, the high current and long-term cycling tests were also conducted (at different current densities of 25 and 50 mA cm^{-2}, each cycle lasted for 60 min). In flexible solid-state batteries, in addition cycling for 30 min (15 min charge and 15 min discharge) at 10 mA cm^{-2}, the cycling measurements were also conducted at 5 mA cm^{-2} for 10 min (5 min charge and 5 min discharge) per cycle. The specific capacity (mAh g$_{Zn}^{-1}$) of aqueous and flexible ZABs at different current densities of 50 and 10 mA cm^{-2} were measured by using the formula: $C = \dfrac{It}{m}$.

Where, C, I, t and m represent specific capacity (mAh g$_{Zn}^{-1}$), current (mA), discharge time (h), and consumed zinc mass (g), respectively.

7. Product analysis

Nuclear magnetic resonance (Ascend 600) was used to analyze the product contents of MOR. First, a series of potassium formate (HCOOK) solutions with the different concentrations (0.5 mM, 1 mM, 1.5 mM, 2 mM, 2.5 mM) were prepared. 500 μL of potassium formate solution and 200 μL of D_2O (deuterium oxide) were added into a NMR tube, and mixed thoroughly for NMR test. A standard curve was drawn based on the proportional relationship between the integrated intensity of the formate ion signal peak and the concentration of formate ion. Typically, for the analysis of the product in the electrolyte, 500 μL of electrolyte and 200 μL of D_2O were added in a NMR tube, and mix them thoroughly. Then the nuclear magnetic resonance test was performed to obtain the integrated intensity of the formate ion signal. The content of formate produced was calculated according to the standard curve [7].
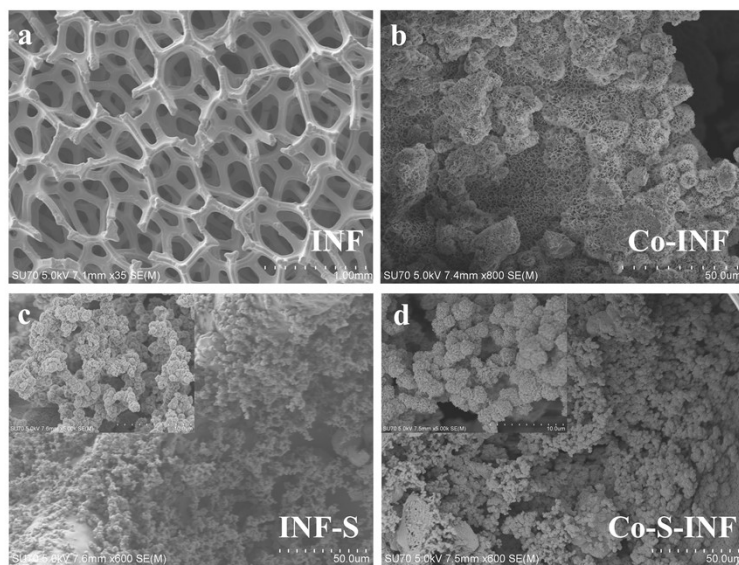
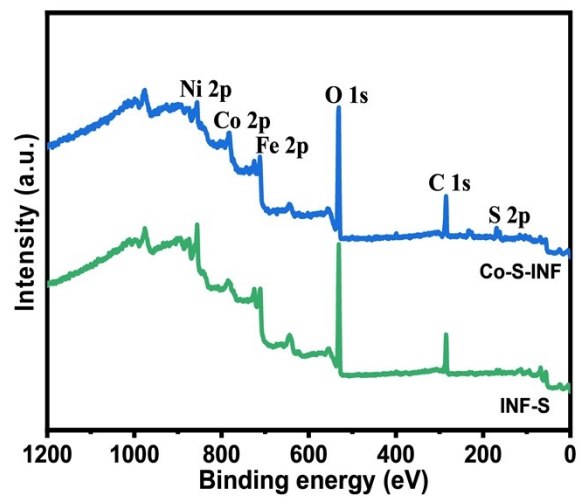**Fig. S1.** SEM images of INF (a), Co-INF (b), INF-S (c), and Co-S-INF (d).

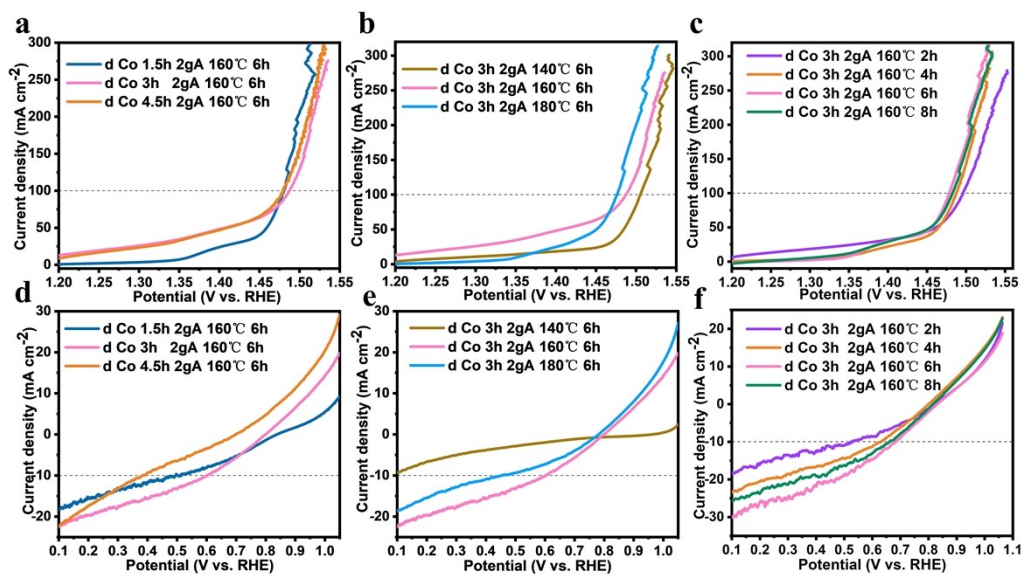**Fig. S2.** XPS spectrum of Co-S-INF and INF-S.

Fig. S3. OER (a) and ORR (d) LSV curves of Co-S-INF synthesized at the different electrodeposition times. OER (b) and ORR (e) LSV curves of Co-S-INF synthesized at different hydrothermal temperatures. OER (c) and ORR (f) LSV curves of Co-S-INF synthesized at different hydrothermal times.
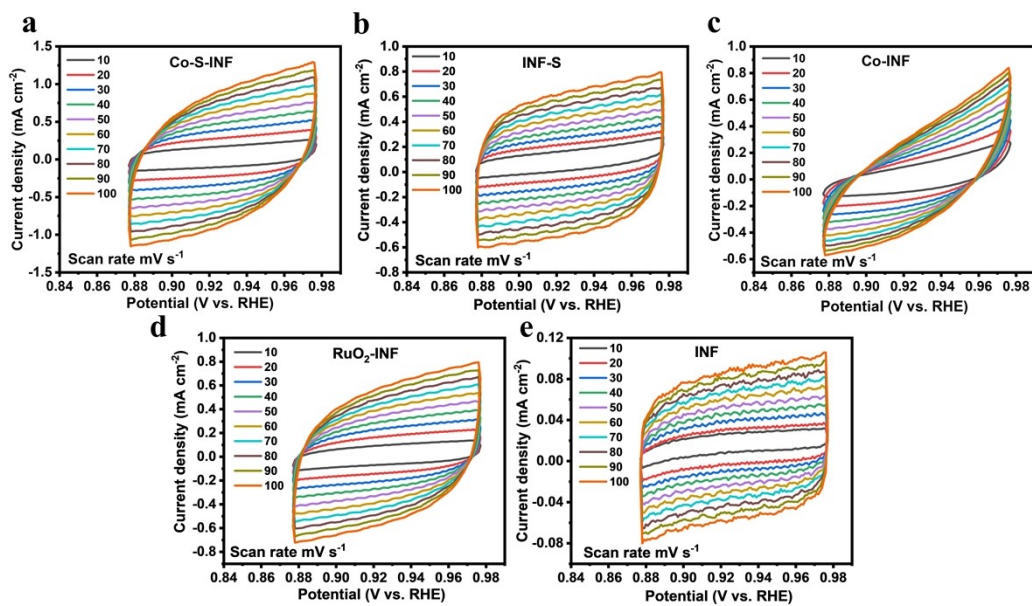
Fig. S4. CV curves of Co-S-INF (a), INF-S (b), Co-INF (c), RuO$_2$-INF (d), and INF

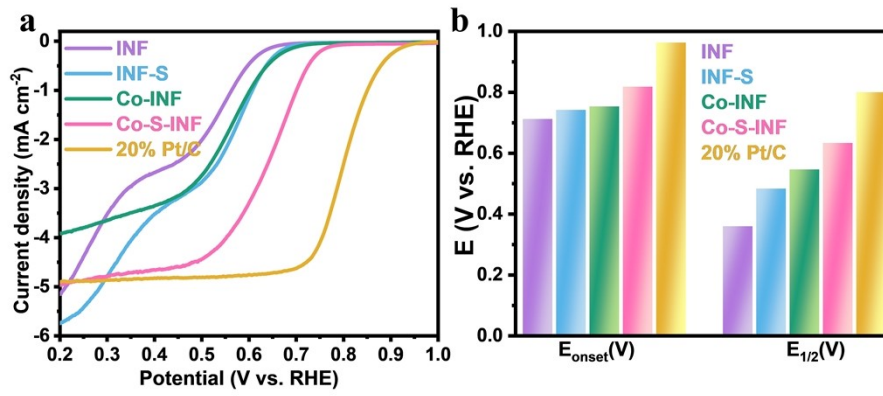(e) at the scan rates of 10-100 mV s^{-1}

Fig. S5. (a) ORR LSV curves of Co-S-INF, INF-S, Co-INF, 20% Pt/C, and INF measured on RDE. (b) E_{onset} and $E_{1/2}$ of Co-S-INF, INF-S, Co-INF, 20% Pt/C, and INF measured on RDE.
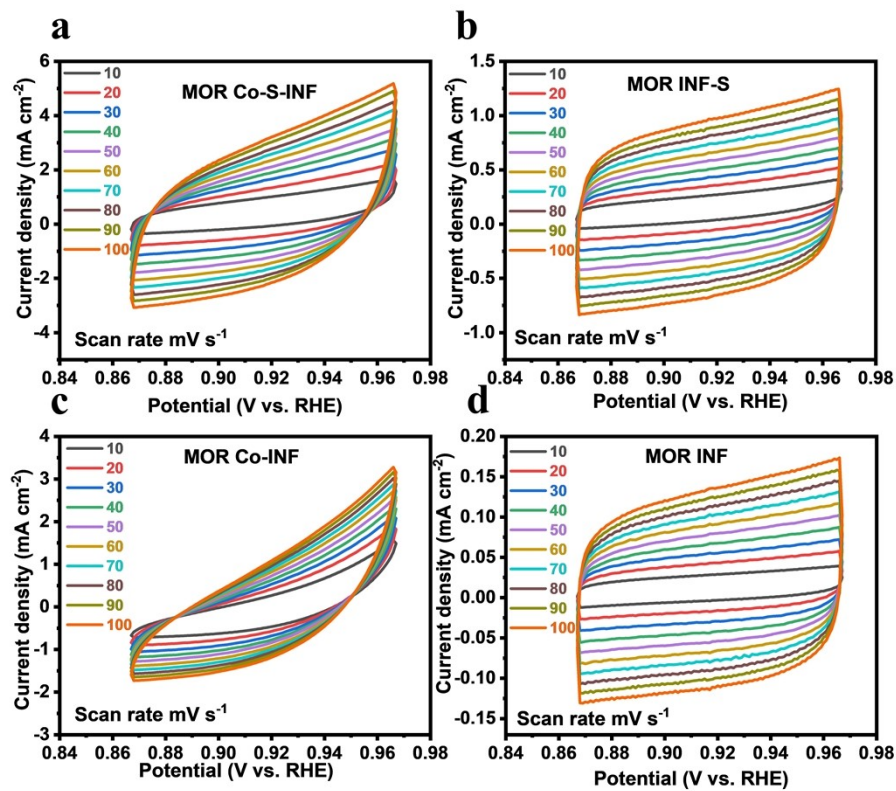
Fig. S6. CV curves of Co-S-INF (a), INF-S (b), Co-INF (c) and INF (d) at scan rates

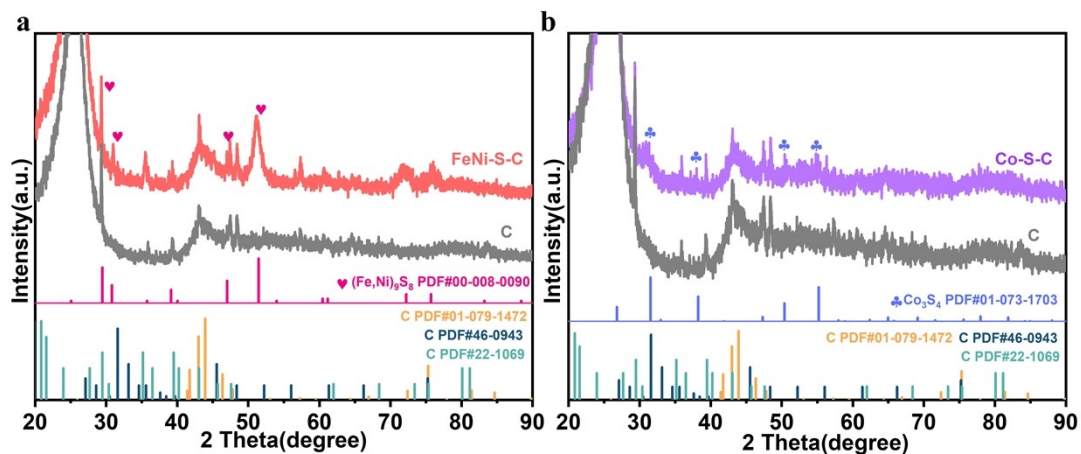of 10-100 mV s^{-1} in 1.0 M KOH + 1.0 M methanol solution.

Fig. S7. XRD patterns of (a) FeNi-S-C and (b) Co-S-C.
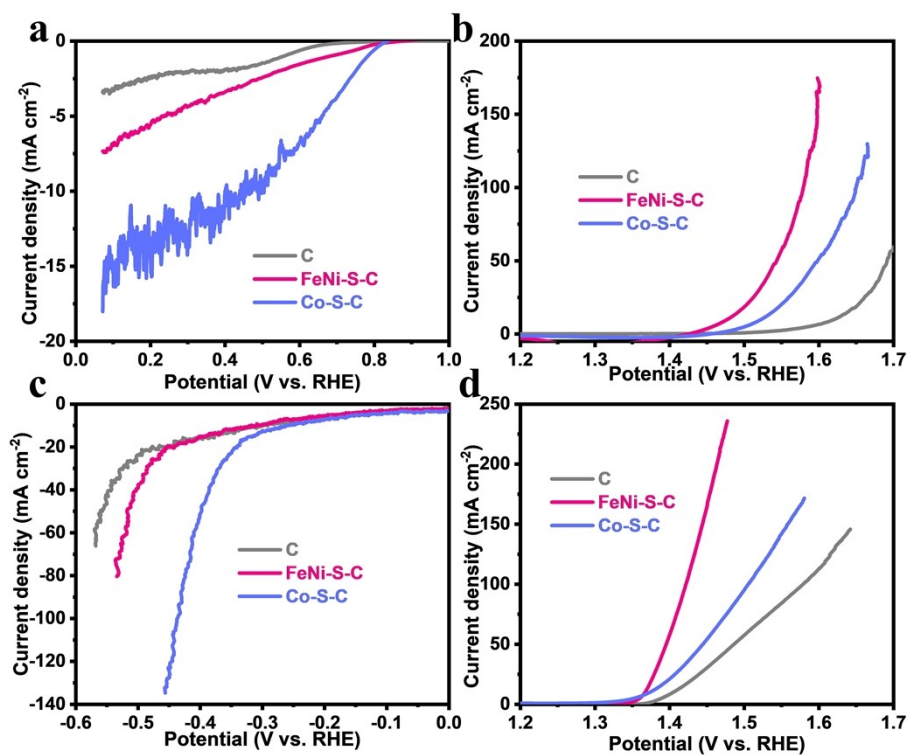
Fig. S8. (a) ORR, (b) OER, (c) HER, (d) MOR LSV curves after iR-compensated of FeNi-S-C, Co-S-C and carbon cloth.

we have synthesized the single Co_3S_4 and $(Fe, Ni)_9S_8$ phases on the inactive carbon cloth substrate, which named as Co-S-C and FeNi-S-C,

respectively (**Fig. S7**), and subsequently tested their LSV curves toward OER, ORR, HER and MOR. As can be seen in **Fig. S8**, the OER and MOR activities of FeNi-S-C are higher than that of Co-S-C. While, the ORR and HER activities of Co-S-C are higher than that of FeNi-S-C.
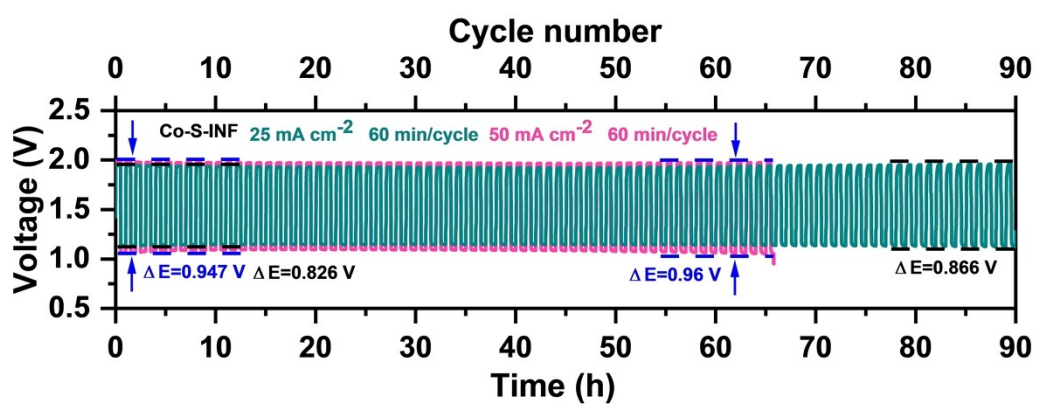
Fig. S9. Cyclic stability curves of the aqueous ZAB with Co-S INF as cathode: 30 min charge and 30 min discharge at 25 mA cm⁻² and 50 mA cm⁻², respectively.
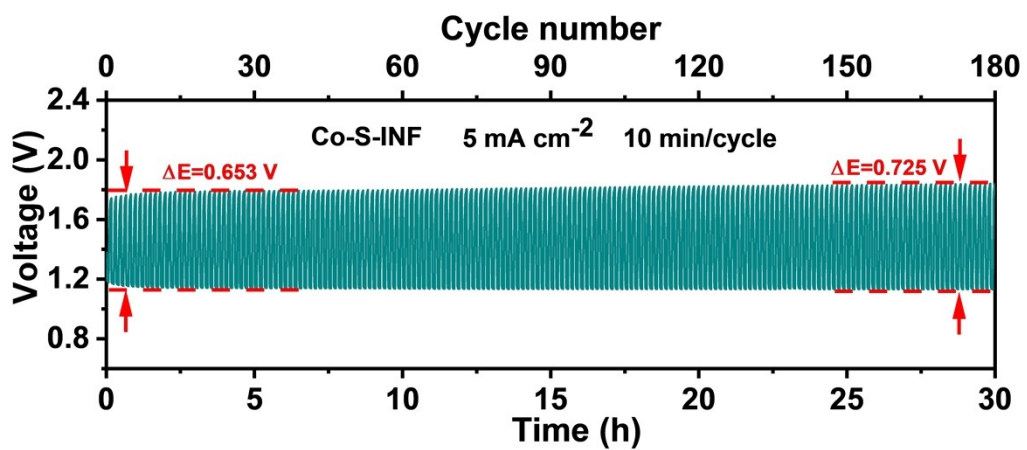
Fig. S10. Cyclic stability curves of the flexible ZAB with Co-S INF as cathode: 5 min charge and 5 min discharge at 5 mA cm^{-2}.
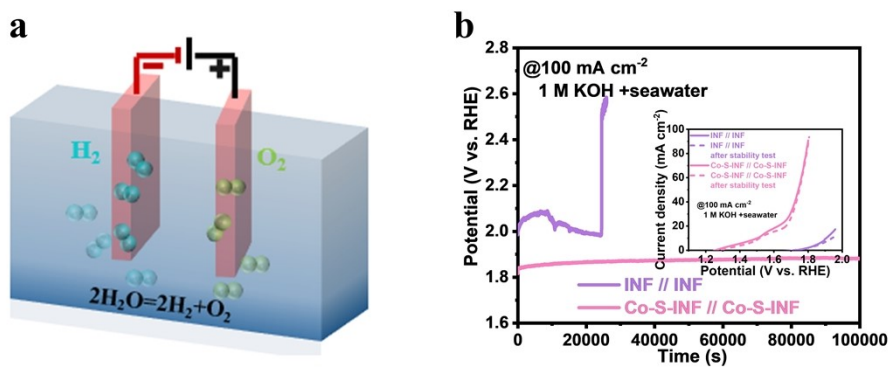
Fig. S11. Schematic illustration of the electrolysis cell with Co-S-INF as both cathode and anode (a). Stability curves of the electrolysis cell with Co-S-INF// Co-S-INF and INF//INF at 100 mA cm^{-2} in the natural seawater. The inset shows polarization curves of overall water splitting before and after stability tests (b).
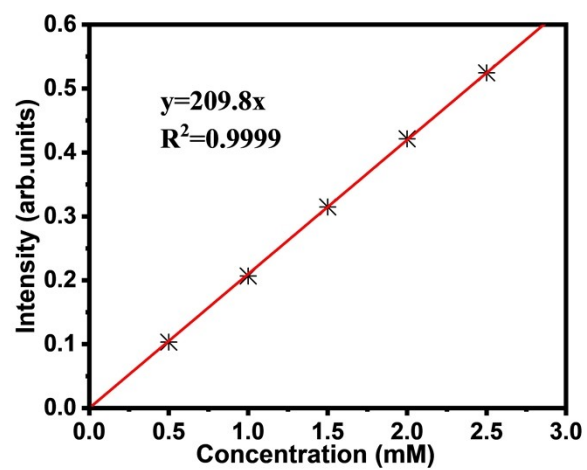
Fig. S12. Standard curve for the formate quantification.

Tab. S1. Co 2p XPS quantitative analyses of Co-S-INF and Co_3O_4.

Samples	Co^{2+}(%)	Co^{3+}(%)	Co^{3+}/Co^{2+}	Average valence of Co
Co-S-INF	44.99%	55.01%	1.22	2.55
Co_3O_4	39.12%	60.88%	1.56	2.61

Tab. S2. Fe 2p XPS quantitative analyses of Co-S-INF and INF-S.

| Samples	Fe^{2+}(%)	Fe^{3+}(%)	Fe^{3+}/Fe^{2+}	Average valence of Fe
Co-S-INF	50.18%	49.82%	0.99	2.50
INF-S	55.97%	44.03%	0.79	2.44

Tab. S3. Ni 2p XPS quantitative analyses of Co-S-INF and INF-S.

Samples	Ni^{2+}(%)	Ni^{3+}(%)	Ni^{3+}/Ni^{2+}	Average valence of Ni
Co-S-INF	55.49%	44.51%	0.80	2.45
INF-S	67.14%	32.86%	0.49	2.33

Tab. S4. Comparisons of the OER catalytic performances of the different metal sulfides including our Co-S-INF.

Samples	solutions	OER overpotential（mV）@100 mA cm^{-2}	References
Co-S-INF	1 M KOH	248	This work
B-TS-H@T-B	1 M KOH	420	[8]
(Ni, Fe)S$_2$@MoS$_2$	1 M KOH	330	[9]
Ni$_3$S$_2$/FeNi$_2$S$_4$-NiFe foam	1 M KOH	239	[10]
Fe$_{0.9}$Ni$_{2.1}$S$_2$@NF	1 M KOH	252	[11]
CuCo-Ni$_3$S$_2$/NF	1 M KOH	400	[12]
Cu@CoS$_x$/Cu Foam	1 M KOH	310	[13]
Ni$_x$Co$_{3-x}$S$_4$/Ni$_3$S$_2$/NF	1 M KOH	320	[14]
Fe$_{0.8}$Ni$_{0.15}$S$_{1.05}$	1 M KOH	330	[15]
Cu$_2$O@Fe-Ni$_3$S$_2$/Cu foam	1 M KOH	250	[16]
Fe-Ni$_3$S$_2$/OXs	1 M KOH	260	[17]

Tab. S5. R_{ct} values of the samples.

Catalysts	R_{ct}/Ω
INF	35.6
INF-S	1.5
Co-INF	2.1
Co-S-INF	1.1
RuO$_2$-INF	17.7

Tab. S6. Property comparisons of ZABs with the Co-S-INF and other reported catalysts.

Electrodes	Peak power density (mW cm^{-2})	Charge/discharge voltage gap (V) @ 100 mA cm^{-2}	Charge/discharge voltage gap (V) @ 200 mA cm^{-2}	References
Co-S-INF	332.3	0.57	1.05	This work
Fe$_1$Co$_1$S$_x$@NSPC	159.0	--	--	[18]
CoMn$_2$O$_4$-S$_2$	108.3	--	--	[19]
CoMn$_{1.5}$Ni$_{0.5}$O$_4$	147.4	1.40	1.90	[20]
BSCCF-NF-H	130.5	1.25	1.65	[21]
Co$_9$S$_8$-FeS$_2$@N-CNFs	214.0	1.40	1.50	[22]
NiCo$_2$Se$_4$/NiCoS$_4$	83.5	1.36	1.87	[23]
Ni$_3$S$_4$@CoS$_x$-NF	143.0	0.69	2.30	[24]
(Fe, Co, Ni)$_9$S$_8$/NSCFs	158	1.29	--	[25]
SNCF-Mn-S$_4$	129.4	1.37	1.87	[26]
CoFe@NC/KB-800	160	0.98	1.42	[27]

Tab. S7. Property comparisons of the flexible solid-state ZABs with the Co-S-INF and other reported catalysts.

Electrodes	Peak power density (mW cm^{-2})	Charge/discharge voltage gap (at 100 mA cm^{-2})	Specific capacity (mAh g$_{Zn}^{-1}$)	References
Co-S-INF	160.5	1.00	778.9	This work
INF-FeCuS	130.0	0.92	777.1	[28]
Fe$_1$Co$_1$S$_x$@NSPC	71.0	--	770.0	[18]
CoFe-SNC	51.5	--	--	[29]
Mn-Ni$_3$S$_2$/NF	75.8	1.42	598.0	[6]
CoMn$_{1.5}$Ni$_{0.5}$O$_4$	85.8	1.25	--	[20]
BSCCF-NF-H	81.7	1.33	705.0	[21]
MnCo$_2$O$_4$	60.3	1.63	--	[30]
Ni$_3$S$_4$@CoS$_x$-NF	100.1	1.22	775.0	[24]
CoxSy/SNC-800	136.0	1.35	777.0	[31]

Tab. S8. Calculation of Faradaic efficiencies of the cathode and anode products in the electrolysis cell with Co-S-INF//Co-S-INF during the alkaline water splitting.

Current density	Time (min)	Theoretical H_2 (mmol)	Detected H_2 (mmol)	Faradaic efficiency (H_2, %)	Theoretical O_2 (mmol)	Detected O_2 (mmol)	Faradaic efficiency (O_2, %)
100 mA cm^{-2}	10	0.311	0.306	98.39	0.156	0.152	97.44
	20	0.622	0.614	98.71	0.311	0.305	98.07
	30	0.933	0.922	98.82	0.466	0.458	98.28
	40	1.244	1.234	99.20	0.622	0.617	99.20
	50	1.555	1.540	99.04	0.777	0.771	99.23
	60	1.866	1.846	98.93	0.933	0.919	98.50

The Faradaic efficiencies of H_2 and O_2 in the electrolysis cell with Co-S-INF as both anode and cathode in 1.0 M KOH electrolyte are measured in a closed electrochemical cell, and the collected H_2 or O_2 gas products are measured by the drainage method. Each collection is repeated at least three times, and the average value is presented. Then, the value of the Faradaic efficiency is calculated based on the following formula [32, 33]：

$$\text{Faraday efficiency} = (m_{\text{Detected}} / m_{\text{Theoretical}}) * 100\%$$

$$m_{\text{Theoretical}} = (I * t) / (n * F)$$

Where the m is the actual mole numbers of the product, n is the number of transferred electrons ($n = 4$ for O_2, $n = 2$ for H_2), F is the Faraday constant ($F=96485.3$ C mol^{-1}), I is current (100 mA cm^{-2}), t is time, and the measurement is at ambient temperature.

Tab. S9. Calculation of Faradaic efficiency of cathode products during the MOR-assisted water splitting.

Current density	Time (min)	Theoretical H_2 (mmol)	Detected H_2 (mmol)	Faradaic efficiency (H_2, %)
	5	0.1555	0.1540	99.04
	10	0.3109	0.3094	99.52
	15	0.4664	0.4603	98.69
	20	0.6219	0.6205	99.77
100 mA cm^{-2}	25	0.7773	0.7723	99.36
	30	0.9328	0.9241	99.07
	35	1.0883	1.0759	98.86
	40	1.2437	1.2277	98.71

The Faradaic efficiency of H_2 produced in the electrolysis cell with Co-S-INF// Co-S-INF in the mixed solution of 1.0 M KOH + 1.0 M methanol is measured in a closed electrochemical cell, and the collected H_2 gas products is measured by the drainage method.

References

[1]   H. Ge, G. Li, J. Shen, W. Ma, X. Meng, L. Xu, Co_4N nanoparticles encapsulated in N-doped carbon box as tri-functional catalyst for Zn-air battery and overall water splitting, Appl. Catal., B. 275 (2020) 119104. https://doi.org/10.1016/j.apcatb.2020.119104.

[2]   D. Chinnadurai, S.J. Lee, Y. Yu, S.Y. Nam, M.Y. Choi, Cation modulation in dual-phase nickel sulfide nanospheres by pulsed laser irradiation for overall water splitting and methanol oxidation reaction, Fuel 320 (2022) 123915. https://doi.org/10.1016/j.fuel.2022.123915.

[3]   H. Deng, C. Zhang, Y. Xie, T. Tumlin, L. Giri, S.P. Karna, J. Lin, Laser induced MoS_2/carbon hybrids for hydrogen evolution reaction catalysts, J. Mater. Chem. A 4 (2016) 6824-6830. https://doi.org/10.1039/c5ta09322h.

[4]   N. Jiang, Q. Tang, M. Sheng, B. You, D. Jiang, Y. Sun, Nickel sulfides for electrocatalytic hydrogen evolution under alkaline conditions: a case study of crystalline NiS, NiS_2, and Ni_3S_2 nanoparticles, Catal. Sci. Technol. 6 (2016) 1077-1084. https://doi.org/10.1039/c5cy01111f.

[5]   F. Zhang, T. Liu, J. Zhang, E. Cui, L. Yue, R. Jiang, G. Hou, The potassium hydroxide-urea synergy in improving the capacitive energy-storage performance of agar-derived carbon aerogels, Carbon 147 (2019) 451-459. https://doi.org/10.1016/j.carbon.2019.03.011.

[6]   M. Yin, H. Miao, B. Chen, R. Hu, L. Xia, C. Zhang, F. Wang, H. Zhang, J. Yuan, Self-supported metal sulfide electrode for flexible quasi-solid-state zinc-air batteries, J. Alloys Compd. 878 (2021) 160434. https://doi.org/10.1016/j.jallcom.2021.160434.

[7]   Y. Qi, Y. Zhang, L. Yang, Y. Zhao, Y. Zhu, H. Jiang, C. Li, Insights into the activity of nickel boride/nickel heterostructures for efficient methanol electrooxidation, Nat. Commun. 13 (2022) 4602. https://doi.org/10.1038/s41467-022-32443-5.

[8] T.T. Li, T.Y. Jing, D.W. Rao, X.T. Jia, Y.P. Zuo, S. Kment, R. Zboril, In situ coating amorphous boride on ternary pyrite-type boron sulfide for highly efficient oxygen evolution, J. Mater. Chem. A 9 (2021) 12283-12290. https://doi.org/10.1039/d0ta10633j.

[9] Y.K. Liu, S. Jiang, S.J. Li, L. Zhou, Z.H. Li, J.M. Li, M.F. Shao, Interface engineering of (Ni, Fe)S_2@MoS_2 heterostructures for synergetic electrochemical water splitting, Appl. Catal., B 247 (2019) 107-114. https://doi.org/10.1016/j.apcatb.2019.01.094.

[10] Y.Y. Wu, Y. Li, M.K. Yuan, H.R. Hao, X.J. San, Z. Lv, L.L. Xu, B. Wei, Operando capturing of surface self-reconstruction of Ni_3S_2/$FeNi_2S_4$ hybrid nanosheet array for overall water splitting, Chem. Eng. J. 427 (2022) 131944. https://doi.org/10.1016/j.cej.2021.131944.

[11] B. Fei, Z.L. Chen, J.X. Liu, H.B. Xu, X.X. Yan, H.L. Qing, M. Chen, R.B. Wu, Ultrathinning nickel sulfide with modulated electron density for efficient water splitting, Adv. Energy Mater. 10 (2020) 2001963. https://doi.org/10.1002/aenm.202001963.

[12] J.F. Qin, M. Yang, S. Hou, B. Dong, T.S. Chen, X. Ma, J.Y. Xie, Y.N. Zhou, J. Nan, Y.M. Chai, Copper and cobalt co-doped Ni_3S_2 grown on nickel foam for highly efficient oxygen evolution reaction, Appl. Surf. Sci. 502 (2020) 144172. https://doi.org/10.1016/j.apsusc.2019.144172.

[13] Y.P. Liu, Q.J. Li, R. Si, G.D. Li, W. Li, D.P. Liu, D.J. Wang, L. Sun, Y. Zhang, X.X. Zou, Coupling sub-nanometric copper clusters with quasi-amorphous cobalt sulfide yields efficient and robust electrocatalysts for water splitting reaction, Adv. Mater. 29 (2017) 1606200. https://doi.org/10.1002/adma.201606200.

[14] Y.Y. Wu, Y.P. Liu, G.D. Li, X. Zou, X.R. Lian, D.J. Wang, L. Sun, T. Asefa, X.X. Zou, Efficient electrocatalysis of overall water splitting by ultrasmall $Ni_xCo_{3-x}S_4$ coupled Ni_3S_2 nanosheet arrays, Nano Energy 35 (2017) 161-170. https://doi.org/10.1016/j.nanoen.2017.03.024.

[15] Z.X. Jing, Q.Y. Zhao, D.H. Zheng, L. Sun, J.H. Geng, Q.N. Zhou, J.J. Lin, Nickel-doped pyrrhotite iron sulfide nanosheets as a highly efficient electrocatalyst for water splitting, J. Mater. Chem. A 8 (2020) 20323-20330. https://doi.org/10.1039/d0ta07624d.

[16] L.L. Wu, Y.X. Yang, X.H. Chen, J. Luo, H.C. Fu, L. Shen, H.Q. Luo, N.B. Li, $Cu_2O@Fe-Ni_3S_2$ nanoflower in situ grown on copper foam at room temperature as an excellent oxygen evolution electrocatalyst, Chem. Commun. (Camb.) 56 (2020) 12339-12342. https://doi.org/10.1039/d0cc04893c.

[17] W. Xu, C. Zhang, H.T. Shen, X.X. Ma, Z.H. Cheng, J. Wu, Q.Z. Zhu, J. Lin, Z.G. Fu, H.Y. Deng, Surface oxalate coordination: facilitating basic OER activity by regulating the electronic structure of $Fe-Ni_3S_2$, ACS Sustainable Chem. Eng. 10 (2022) 14396-14406. https://doi.org/10.1021/acssuschemeng.2c02456.

[18] W. Fang, P. Dai, H. Hu, T. Jiang, H. Dong, M. Wu, $Fe_{0.96}S/Co_8FeS_8$ nanoparticles co-embedded in porous N, S codoped carbon with enhanced bifunctional electrocatalystic activities for all-solid-state Zn-air batteries, Appl. Surf. Sci. 505 (2020) 144212. https://doi.org/10.1016/j.apsusc.2019.144212.

[19] Z. Zhang, H. Sun, J. Li, Z. Shi, M. Fan, H. Bian, T. Wang, D. Gao, S-doped $CoMn_2O_4$ with more high valence metallic cations and oxygen defects for zinc-air batteries, J. Power Sources 491 (2021) 229584. https://doi.org/10.1016/j.jpowsour.2021.229584.

[20] B. Chen, H. Miao, M. Yin, R. Hu, L. Xia, C. Zhang, J. Yuan, Mn-based spinels evolved from layered manganese dioxides at mild temperature for the robust flexible quasi-solid-state zinc-air batteries, Chem. Eng. J. 417 (2021) 129179. https://doi.org/10.1016/j.cej.2021.129179.

[21] X.Y. Wu, H. Miao, M.M. Yin, R.G. Hu, F. Wang, H.C. Zhang, L. Xia, C.F. Zhang, J.L. Yuan,

Biomimetic construction of bifunctional perovskite oxygen catalyst for zinc-air batteries, Electrochim. Acta 399 (2021) 139407. https://doi.org/10.1016/j.electacta.2021.139407.

[22] L. Sun, S. Huang, X. Zhao, L. Li, X. Zhao, W. Zhang, Synergistic effect of Co_9S_8 and FeS_2 inlaid on N-doped carbon nanofibers toward a bifunctional catalyst for Zn-air batteries, Langmuir 38 (2022) 11753-11763. https://doi.org/10.1021/acs.langmuir.2c01882.

[23] K.K. Wang, Z.S. Lin, Y. Tang, Z.H. Tang, C.L. Tao, D.D. Qin, Y. Tian, Selenide/sulfide heterostructured $NiCo_2Se_4/NiCoS_4$ for oxygen evolution reaction, hydrogen evolution reaction, water splitting and Zn-air batteries, Electrochim. Acta 368 (2021) 137584. https://doi.org/10.1016/j.electacta.2020.137584.

[24] M. Yin, H. Miao, J. Dang, B. Chen, J. Zou, G. Chen, H. Li, High-performance alkaline hybrid zinc batteries with heterostructure nickel/cobalt sulfide, J. Power Sources 545 (2022) 231902. https://doi.org/10.1016/j.jpowsour.2022.231902.

[25] T. Jiang, P. Dai, W. Zhang, M. Wu, Fish bone-derived N, S co-doped interconnected carbon nanofibers network coupled with (Fe, Co, Ni)$_9$S$_8$ nanoparticles as efficient bifunctional electrocatalysts for rechargeable and flexible all-solid-state Zn-air battery, Electrochim. Acta 373 (2021) 137903. https://doi.org/10.1016/j.electacta.2021.137903.

[26] J. Zou, D. Qiu, G. Chen, H. Miao, J. Dang, L. Xia, Q. Wang, H. Zhang, J. Yuan, Greatly enhancing the bifunctional oxygen catalytic activities of cobalt-based perovskites by anchoring metal sulfides, J. Alloys Compd. 933 (2023) 167817. https://doi.org/10.1016/j.jallcom.2022.167817.

[27] S. Ren, X. Duan, F. Ge, Z. Chen, Q. Yang, M. Zhang, H. Zheng, Novel MOF-derived hollow CoFe alloy coupled with N-doped ketjen black as boosted bifunctional oxygen catalysts for Zn–air batteries, Chem. Eng. J. 427 (2022) 131614. https://doi.org/10.1016/j.cej.2021.131614.

[28] J.X. Dang, M.M. Yin, D.H. Pan, Z.Q. Tian, G.M. Chen, J.Q. Zou, H. Miao, Q. Wang, J.L. Yuan, Four-functional iron/copper sulfide heterostructure for alkaline hybrid zinc batteries and water splitting, Chem. Eng. J. 457 (2023) 141357. https://doi.org/10.1016/j.cej.2023.141357.

[29] C.-C. Weng, J.-T. Ren, H.-Y. Wang, X.-W. Lv, Y.-J. Song, Y.-S. Wang, L. Chen, W.-W. Tian, Z.-Y. Yuan, Triple-phase oxygen electrocatalysis of hollow spherical structures for rechargeable Zn-Air batteries, Appl. Catal., B 307 (2022) 121190. https://doi.org/10.1016/j.apcatb.2022.121190.

[30] J. Zou, B. Chen, B. Li, M. Yin, H. Miao, F. Wang, C. Zhang, H. Zhang, J. Yuan, Achieving high energy efficiency of alkaline hybrid zinc battery by using the optimized Co–Mn spinel cathode, Int. J. Hydrogen Energy 47 (2022) 27470-27480. https://doi.org/10.1016/j.ijhydene.2022.06.082.

[31] Z. Yang, J. Gao, P. Zhu, X. Zhao, G. Wang, S. Liu, Encapsulated Co_xS_y nanoparticles decorated S, N-doped mesoporous carbon as effective bifunctional oxygen electrocatalyst in rechargeable Zn-air battery, J. Alloys Compd. 858 (2021) 157665. https://doi.org/10.1016/j.jallcom.2020.157665.

[32] R. Li, X.J. Liu, W.H. Liu, Z.B. Li, K.C. Chan, Z.P. Lu, Design of hierarchical porosity via manipulating chemical and microstructural complexities in high-entropy alloys for efficient water electrolysis, Adv. Sci. 9 (2022) 2105808. https://doi.org/10.1002/advs.202105808.

[33] R.G. Hu, F.Y. Liu, H.Q. Qiu, H. Miao, Q. Wang, H.C. Zhang, F. Wang, J.L. Yuan, High-property anode catalyst compositing Co-based perovskite and NiFe-layered double hydroxide for alkaline seawater splitting, Processes 10 (2022) 668. https://doi.org/10.3390/pr10040668.